esteem3

Enabling Science through European Electron Microscopy

Second report on TEM methods applied to materials for transport

Deliverable D10.2 – version 1

Estimated delivery date: 1 Dec 2021

Actual delivery date: 3 Dec 2021

Lead beneficiary: KRA, TRO

Person responsible: Adam Kruk, Randi Holmestad

Deliverable type: ☒ R ☐ DEM ☐ DEC ☐ OTHER ☐ ETHICS ☐ ORDP

Dissemination level: ☒ PU ☐ CO ☐ EU-RES ☐ EU-CON ☐ EU-SEC

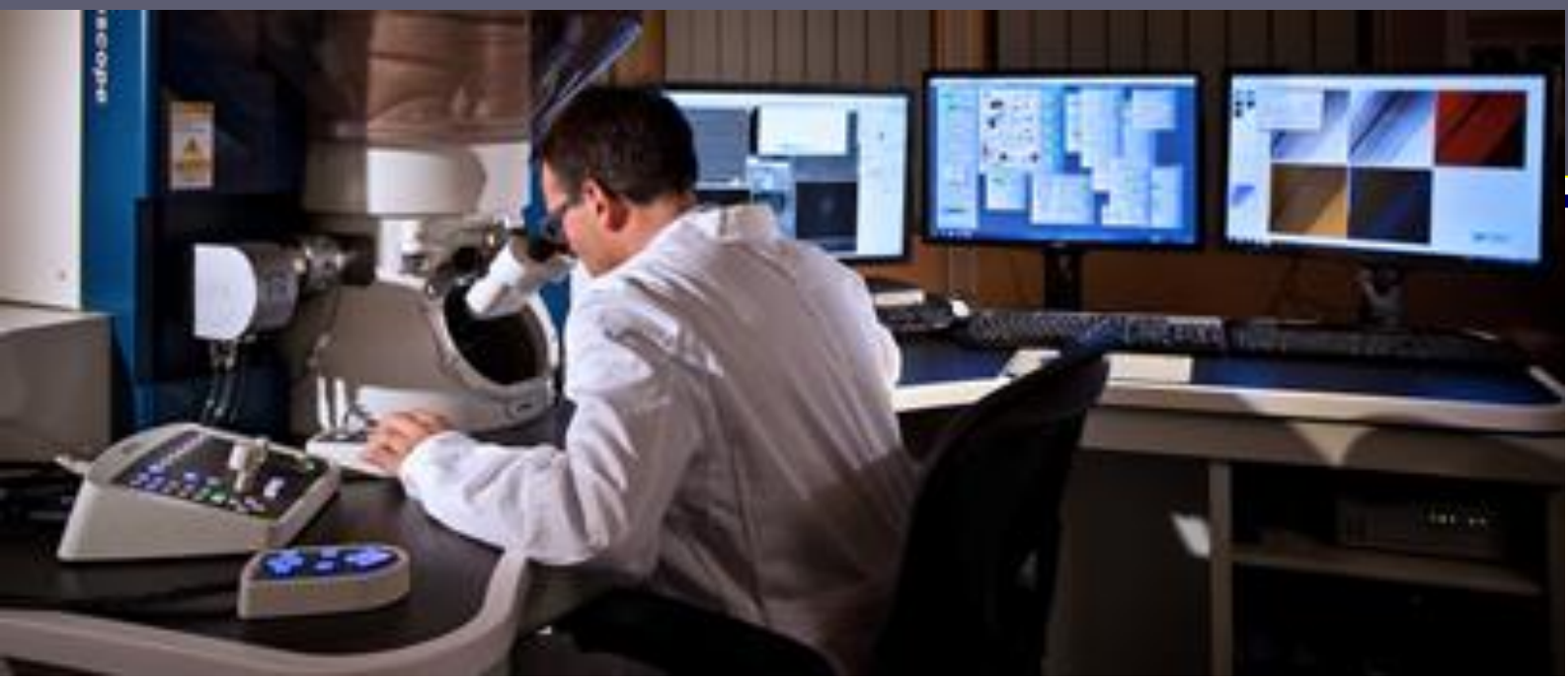

THIS PROJECT HAS RECEIVED FUNDING FROM THE EUROPEAN UNION'S HORIZON 2020 RESEARCH AND INNOVATION PROGRAMME UNDER GRANT AGREEMENT NO **823717**

Grant Agreement No:	823802
Funding Instrument:	Research and Innovation Actions (RIA)
Funded under:	H2020-INFRAIA-2018-1: Integrating Activities for Advanced Communities
Starting date:	01.01.2019
Duration:	54 months

Table of contents

Revision history log

Version number	Date of release	Author	Summary of changes
V0.1	24.11.2021	Adam Kruk (KRA)	Contributed KRA parts on the report
V0.2	1.12.2021	Dipanwita Chatterjee (TRO)	Added parts from TRO on the report
V0.3	3.12.2021	Randi Holmestad and Dipanwita Chatterjee (TRO)	Added small parts and finalized the draft
V.1	3.12.2021	Peter A. van Aken	Approval of document
V.1	3.12.2021	Aude Garsès	General review

Task 10.1 : Sample preparation for materials for transport (TRO, KRA)

The aim of this task is the implementation of sample preparation methods for various "difficult" materials such as Ni-based superalloys, advanced high-strength steels (AHSS), Ti, Al and Mg-based alloys and fibre reinforced composite materials using different techniques for preparing thin artefact free TEM lamellae. High quality, electron transparent samples are essential for state-of-the-art TEM/STEM/SPED/ in situ investigations. Optimization of the available techniques of sample preparations like tripod polishing, ion milling, FIB techniques, electro polishing have been conducted depending on the requirement of the material and the design of the experiment. New techniques for preparing sensitive samples were investigated and protocols for sample preparation were prepared and published online on ESTEEM3 website last year. Since then, work on the sample characterization has progressed. No new advancement in terms of sample preparation was made.

Task 10.2 : Materials for Aeronautics/Aerospace (TRO, KRA, TOU)

Microstructural studies of nickel-based superalloy (KRA)

This task presents the results of applying analytical TEM and FIB-SEM tomography techniques to perform detailed characterization (visualization in 3D, quantification and phases identification) of structural elements in various engineering materials. The KRA team investigated materials' structure and phase morphology due to their application for aeronautics, including Ni-base superalloy Inconel 718 and Allvac 718Plus; those results are described and presented below.

The 718Plus is a relatively new polycrystalline nickel-based superalloy designed to replace the widely used superalloys in some applications such as Waspaloy and Inconel 718 superalloys. It combines excellent mechanical properties with oxidation resistance and workability, making it suitable for application in critical rotating components in gas turbines used in aircraft and the energy industry.

Inconel 718 and ATI 718Plus belong to a group of precipitation-hardened Ni-base superalloys. The alloys mentioned above feature high strength and excellent corrosion resistance combined with relatively good weldability. Fusion welding leads to micro-segregation during weld metal solidification. This phenomenon may result in the formation of low melting temperature eutectics and brittle phases in the inter-dendritic regions of the fusion zone. These microstructural constituents have an important effect on the mechanical properties of the welded joint. Allvac 718Plus (718Plus) is a high strength, corrosion-resistant nickel-based superalloy designed to replace Inconel 718 superalloy (IN718) in some applications in the power generation and aerospace industry. In comparison to IN718, the 718Plus shows improved temperature performance. Its chemical composition is Ni-18-Cr-10-Fe-9Co-5.1(Nb+Ta)-1W-2.7Mo-0.8Ti-1.5Al-00.3C (wt %). The post welded heat treatment leads to (γ'-Ni3(Al,Ti) precipitation in all alloy volume and platelet precipitates of η-Ni3Ti phases nucleating at the Laves phase. The microstructure of the fusion zone consists of a γ dendrite matrix with two kinds of eutectics: (MC–type carbides + γ phase) and (Laves-phase + η-phase) precipitates in the inter-dendritic region.

Specific challenges include identifying and detailed characterization at the nanoscale of various advanced structural and functional materials, implementing different diffraction, spectroscopy and data analysis techniques. The high-resolution SEM and TEM application to a detailed characterization of structural elements in EBW dissimilar Inconel 718/Allvac 718Plus welded joint. The effects of welding and post

welding heat treatment on the microstructure of the fusion zone of Inconel 718/Allvac 718Plus welded joint was analyzed.

Figure 10.2.1 presents the result of applying the FIB-SEM tomography technique for visualization in 3D of the delta phase precipitates and strengthening the gamma bis phase precipitates for the Inconel 718 superalloy after standard heat treatment. The visualization revealed dislocations in the γ phase thanks to the precipitation of the γ″- phase that separated them. The conducted analysis allowed quantitatively parameterizing the precipitation particles of phases to determine their spatial distribution, which is impossible to carry out using TEM methods. This approach to structural testing provides for a complete structural assessment of construction materials. The conducted analysis of the high-resolution STEM of the γ″phase precipitates in the Inconel 718 superalloy after standard heat treatment allowed us to visualize the distribution of Nb atoms in the γ″ phase to determine the coherence with the γ matrix of these precipitates. The results of this analysis are presented in Fig. 10.2.2.

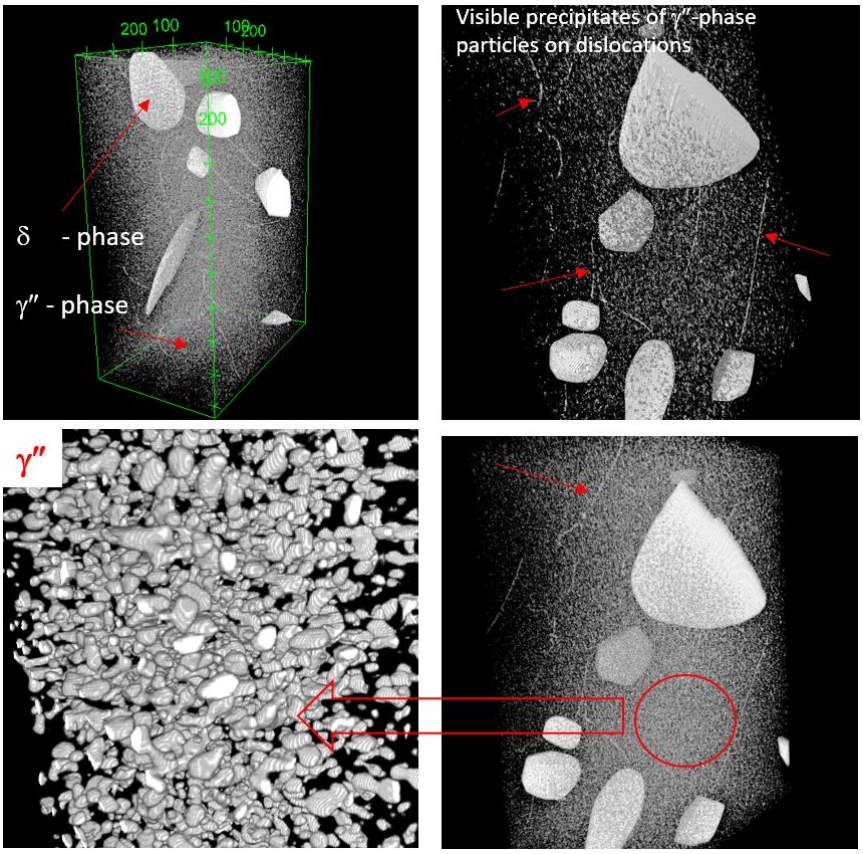

Figure 10.2.1. 3D visualization of delta phase precipitates and enhancing γ″ precipitates for Inconel 718 superalloy after standard heat treatment.

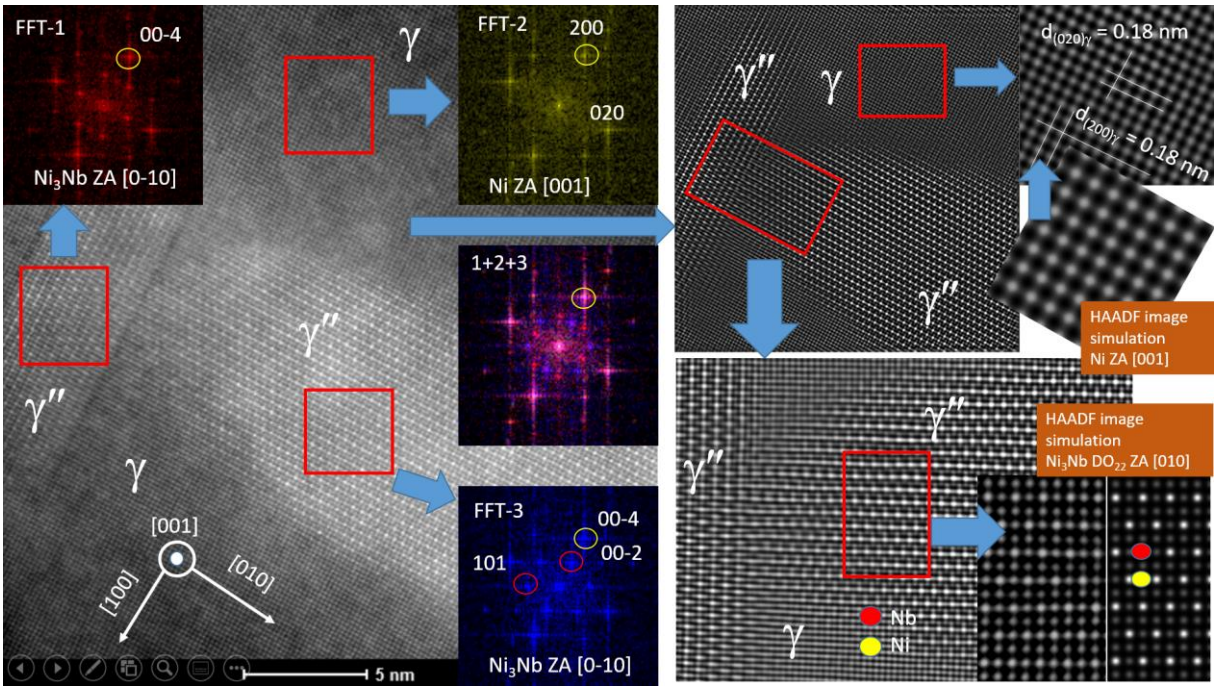

Figure 10.2.2. High-resolution STEM analysis of γ″ phase precipitates in Inconel 718 superalloy after standard heat treatment.

The presented results aimed to analyze the Laves phase transformation in the fusion zone of the electron beam welded dissimilar Inconel 718/Allvac 718Plus joint during exposure at 760 °C. FIB-SEM tomography was employed to reveal the shape and spatial distribution of selected microstructural features within the weld metal. Visualization in 3D of the tomographic reconstructed volume of a region chosen from the fusion zone after exposure at 760 °C for 500h was presented in Fig.10.2.3. For 3D visualization of precipitates, a FIB-SEM technique was employed utilizing NEON CrossBeam 40EsB (ZEISS, Germany) microscope with Ga-ion beam. In-lens, secondary- and Energy-selective Backscattered (EsB) electron images were obtained using a beam 1.5 kV and 50 pA parameters. In-situ milling was conducted using an ion beam operating at 30 kV, 50 pA with 30 µm aperture. Tomographic reconstruction was prepared as follows: at first, the region of interest (ROI) was identified by SEM imaging and coated by a protective platinum layer to prevent any negative preparation effects, such as curtaining effect, and make the further process more stable. The stack of 146 SEM images (image size 1024 x 768 pixels, 8-bit grayscale, stack size 113 MB) was acquired from the cross-section of the investigated sample. Sequential removal of 8 nm layers allowed to receive 7.25 x 3.62 x 6.32 µm (V = 165.9 µm3) total volume for further analysis and reconstruction with a voxel size of 8 × 8 × 8 nm. All the data processing, including image shift corrections, image analysis and 3D visualizations, were performed using open source Fiji software. The same image analysis was applied for each image in the reconstructed stack, even though the contrast in some slices was slightly different. This approach allowed minimizing the subjective analysis factor. The nearest-neighborhood algorithm was used for object segmentation; thus, nearby voxels with the same and similar grey levels were assigned to one object. 3D visualization of the reconstructed volume was done using Avizo Fire 6.3 software (ThermoFisher, USA).

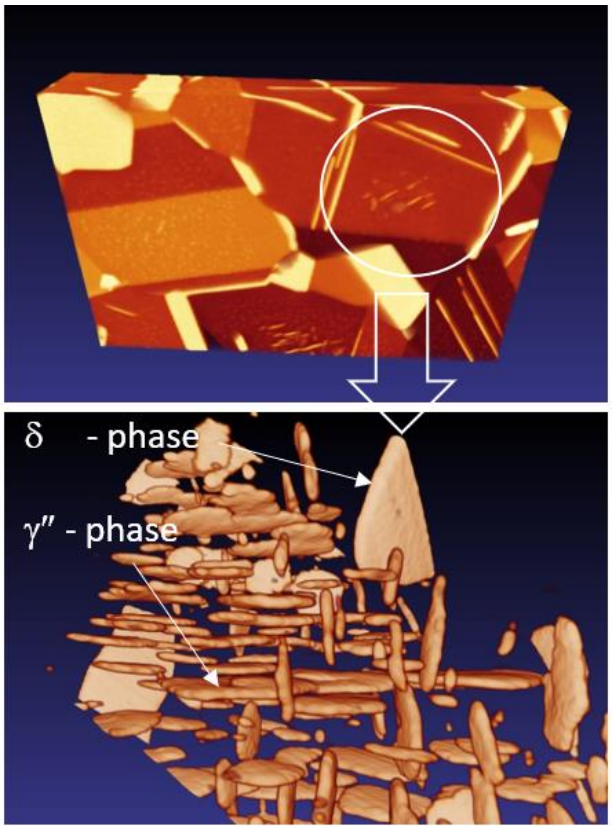

Figure 10.2 3. Visualization in 3D the γ″ particles in base material IN718 after standard heat treatment and long-time annealing at 760 °C for 500 h.

This work presents results of the application of various research methods and techniques to the analysis of phases resulting from the transformation of the Laves phase during long-term annealing. Laves phase transformation within the fusion zone of Inconel 718/Allvac 718Plus EB welded joint during elevated temperature exposure.

The investigations were performed using scanning electron microscopy (SEM) and high-resolution scanning transmission electron microscopy (HRSTEM) supported by energy-dispersive X-ray spectroscopy (XEDS). To identify phases present in the weld metal before and after isothermal hold, selected area electron diffraction (SAED) supported by Java Electron Microscopy Software (JEMS 4.81) was used. The fusion zone in the as-welded condition has an as-cast structure with dendrites of the γ matrix surrounded by interdendritic regions consisting of MC-type carbides and Laves phase precipitates within the γ matrix. Exposure of the welded joint at 649 and 760 °C prompted a string of microstructural changes in the fusion zone. Reprecipitation and growth of main strengthening phases' particles occurred. Figure 10.2.4 presents results of the chemical composition of individual phases (γ, γ′, σ, η) investigations of post welded heat treatment (PWHT) in the fusion zone (760 °C / 500 h) using STEM-XEDS technique.

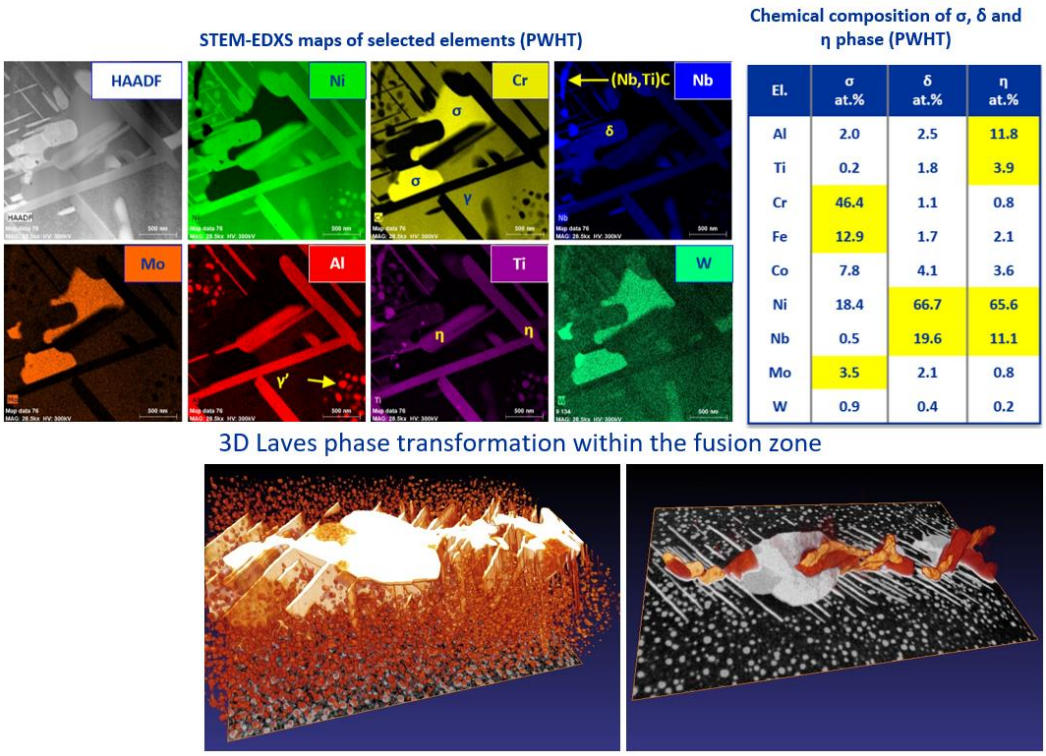

Figure 10.2.4. Chemical composition of individual phases (γ, γ′, σ, η) investigations of post welded heat treatment (PWHT) in the fusion zone (760 °C / 500 h) using STEM-XEDS. Additionally, results of 3D visualization of the analyzed region were presented.

The selected results of the application of 3D imaging technique for microstructural elements visualization, their shape determination, spatial distribution and quantification, as well as STEM - EDX technique for determining the chemical composition of selected structural elements in the fusion zone of the EBW Inconel 718 / Allvac 718PLUS, welded joint after PWHT at 649 °C / 500 h were presented in Figure 10.2.5.

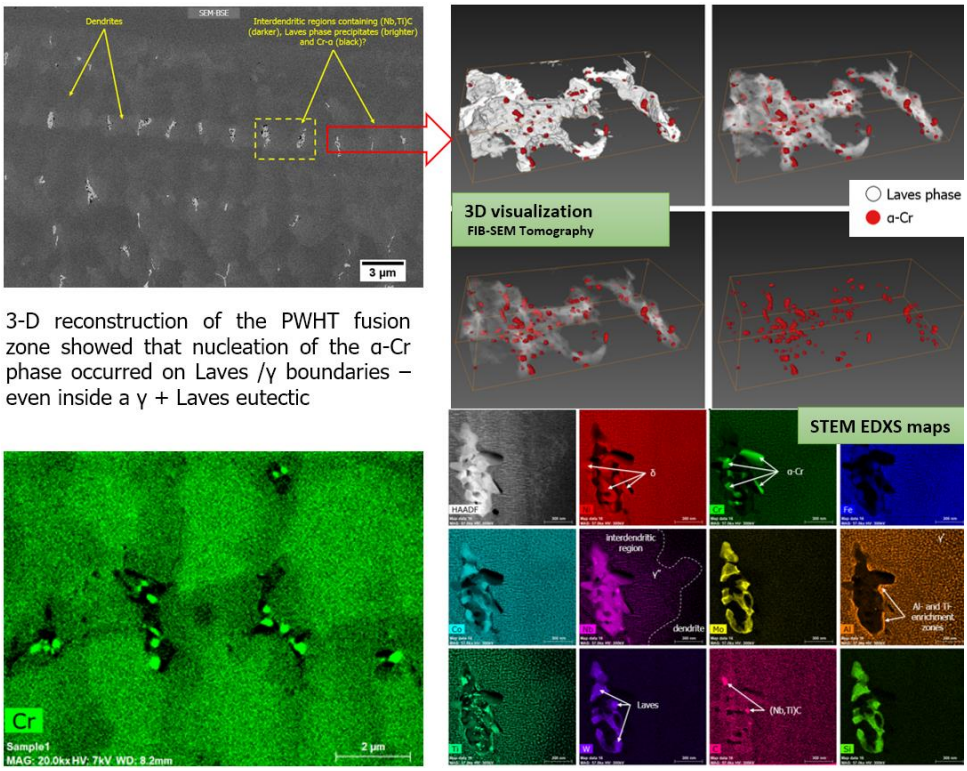

Figure 10.2.5. The application of 3D visualization and TEM (STEM-HAADF, SAED, STEM - EDX) techniques to characterize the morphology, spatial distribution, and chemical composition of selected structural elements in the fusion zone of the EBW Inconel 718 / Allvac 718PLUS welded joint. FIB-SEM Tomography of the PWHTed fusion zone (649 °C / 500 h).

Figure 10.2.5 presents SEM microphotographs of the fusion zone and shows the phase transformation in the fusion during exposure at 640 °C and 760 °C. 3D reconstruction of the PWHT fusion zone showed that nucleation of the α-Cr phase occurred on Laves /γ boundaries – even inside a γ + Laves eutectic (Fig.10.2.6).

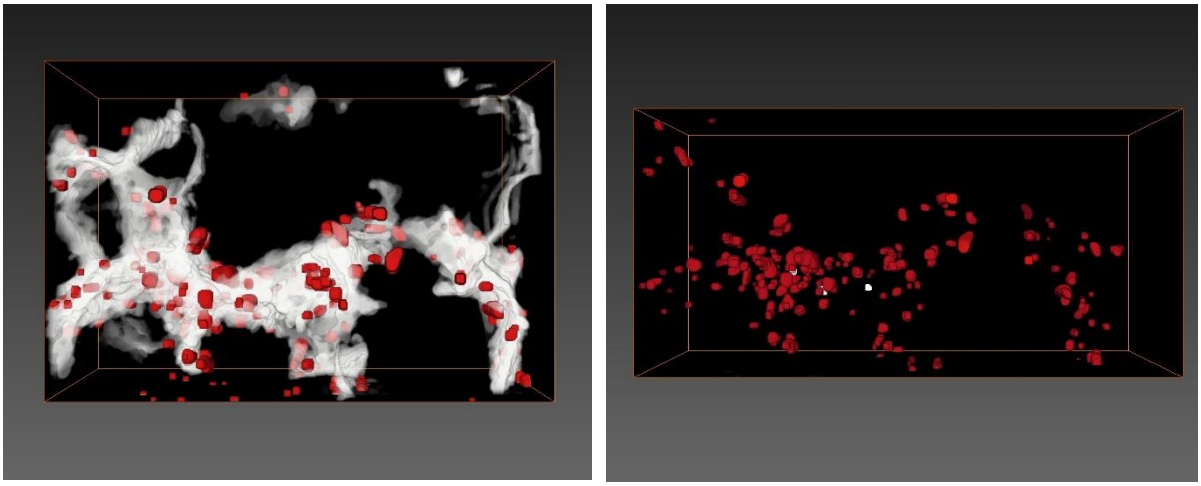

Figure 10.2.6. 3D reconstruction of the PWHT fusion zone showed that nucleation of the α-Cr phase occurred on Laves /γ boundaries – even inside a γ + Laves eutectic.

The TEM lamella was cut using *combining FIB-SEM tomography* with purposeful sampling from the analyzed sample volume. FIB-SEM Tomography of the PWHTed fusion zone (649 °C / 500 h). The results of the high-resolution HRSTEM analysis of the tomographically reconstructed Cr precipitates are presented in Fig. 10.2.7.

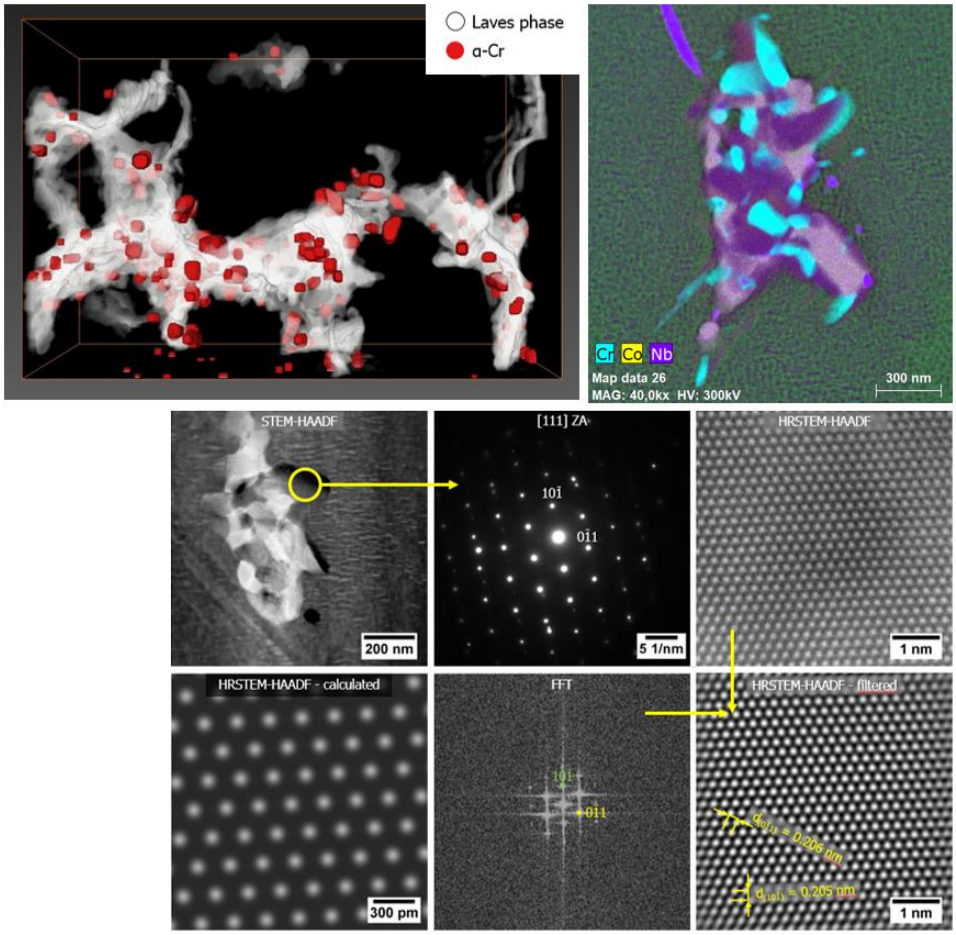

Figure 10.2.7. Visualization and HRSTEM analysis of α-Cr precipitates formed during long-term annealing of the joint material at the temperature of 649 °C for 500 hours.

Based on the obtained results, the spatial distribution of the analyzed precipitates was shown, and their chemical composition was also determined. Diffraction and high-resolution analysis confirmed that the analyzed precipitates are α-Cr particles. In comparison to an area of the dendrite (D) selected area, electron diffraction from the inter-dendritic region (IR) of the fusion zone revealed additional spots from γ" phase (yellow arrows). The results of the high-resolution HRSTEM analysis of the tomographically reconstructed α-Cr precipitates are presented in Fig. 10.2.8.

The results of the TEM-SAED analysis from the inter-dendritic areas of the weld subjected to heat treatment at 649 C for 500 h confirming the presence of the precipitates of the gamma bis strengthening phase in the vicinity of the complex separation of which the tomographic reconstruction is shown in Fig. 10.2.8.

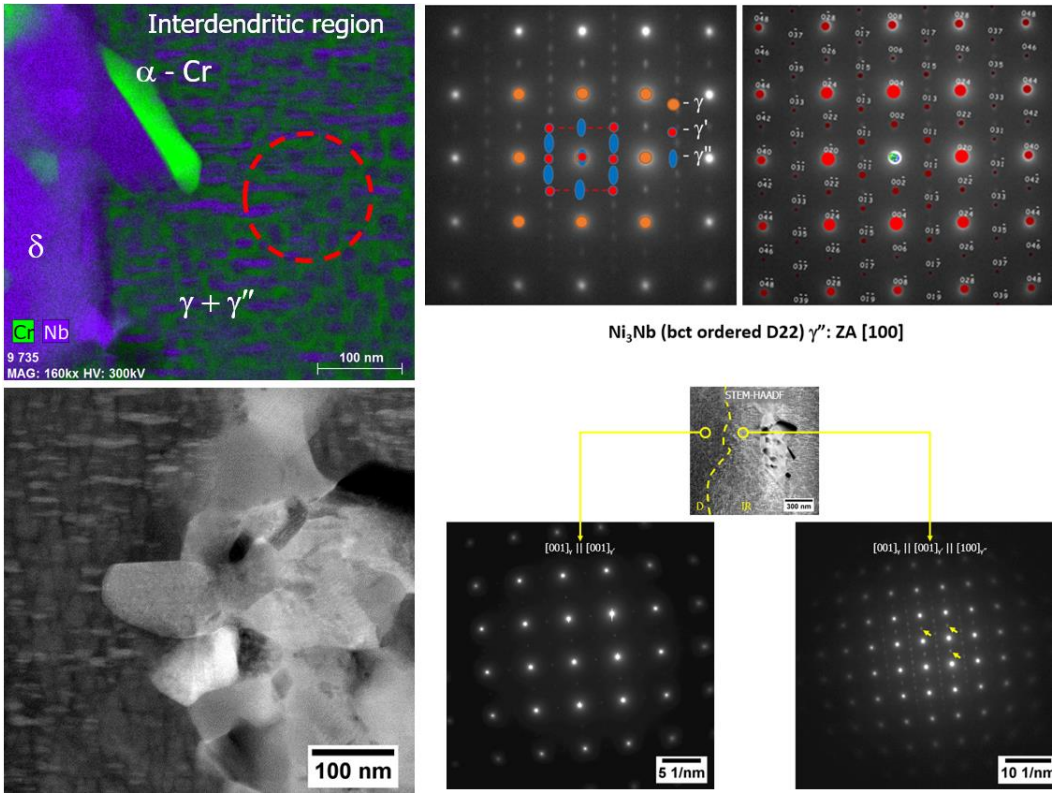

Figure 10.2.8. TEM-SAED analysis from the inter-dendritic areas of the weld after heat treatment at 649 °C for 500 h.

Comparative tests to illustrate of influence of the increased annealing temperature on the stability of the weld structure, of the weld areas in the state after welding and after heat treatment were carried out. The results of TEM analysis confirmed the presence of the Laves phase precipitates in the inter-dendritic regions after welding (Fig.10.2.9) and the disintegration of this phase during post-welding treatment at 760 °C for 500 h, (Fig.10.2.10).

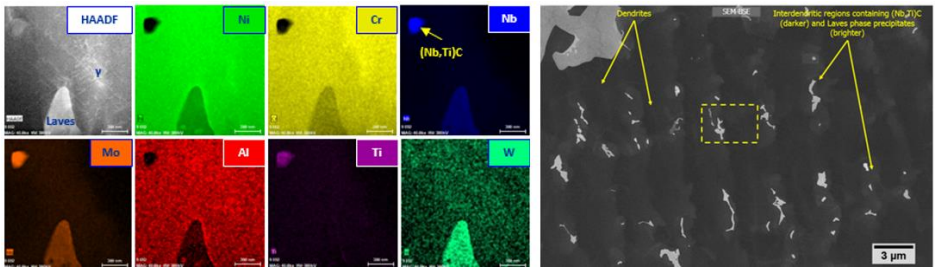

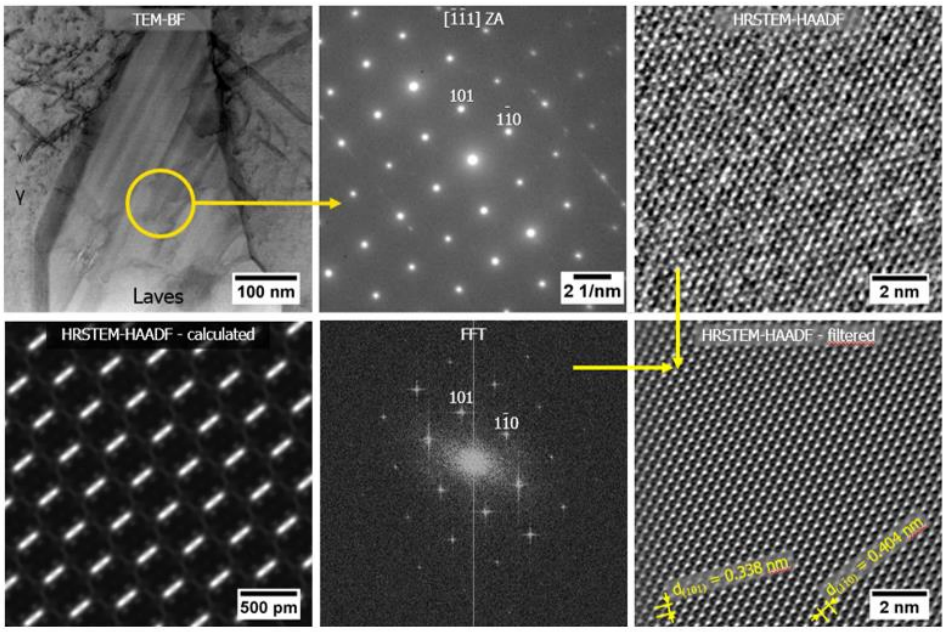

Figure 10.2.9. TEM/HRSTEM analysis of the lamella from the fusion zone after post-welding treatment at 760 °C for 500 h.

Furthermore, a transformation of the Laves phase to a complex cluster of precipitates enclosed both μ and σ phases had taken place. Precipitates enriched in Mo and W were identified as trigonal μ phase, whereas other areas enriched in Mo, W and Cr – as tetragonal σ phase. Moreover, plate-like precipitates of δ/η phases growing from the complex cluster of precipitates' surfaces were observed (Fig. 10.2.10).

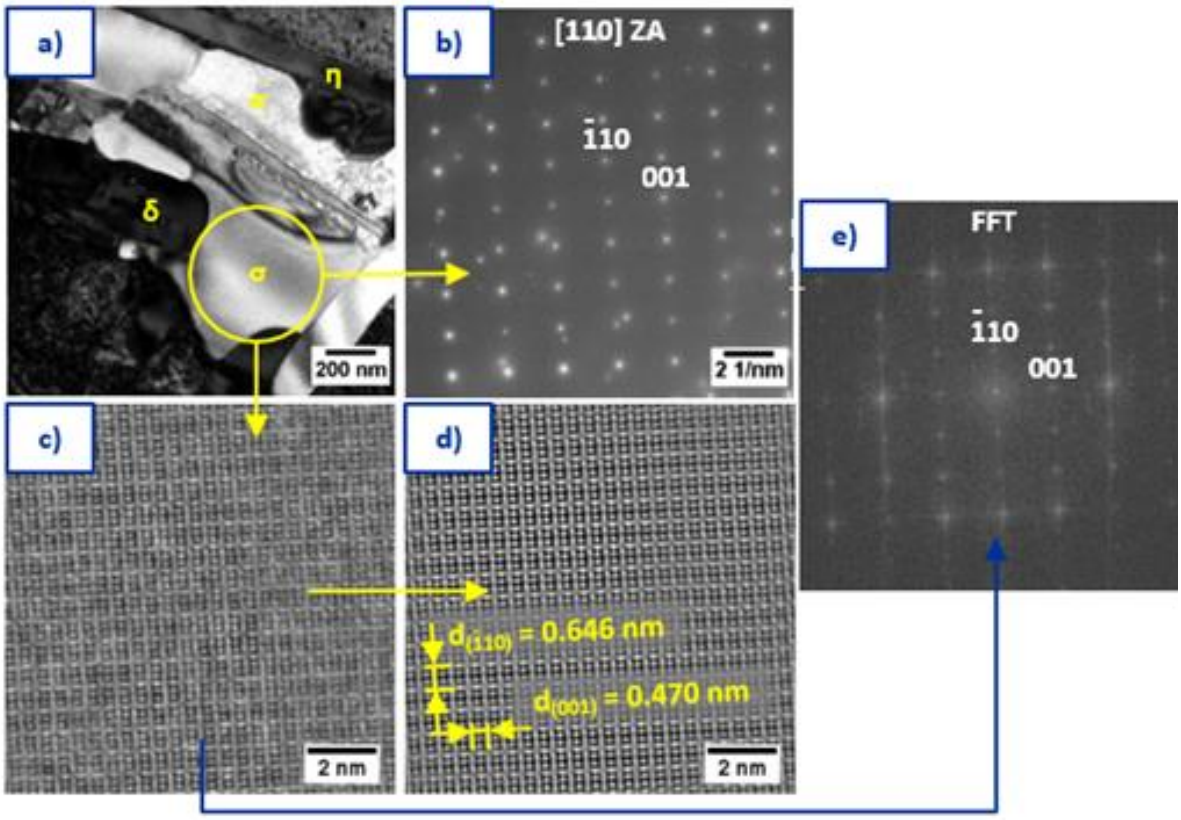

Figure 10.2.10. TEM/HRSTEM analysis of the lamella from the fusion zone in the as-welded condition.

Detonation nanodiamond (DND) particles (KRA)

Applications of DND for various devices in transport:

- Supercapacitors
- Batteries
- Electrocatalysis
- Optoelectronics
- Thermoelectric
- Nanofluids
- Water treatment

Detonation diamond (DND) nanoparticles have promising applications ranging from lubrication and polishing to biotechnology and electronics. However, the physical and chemical properties of the surface of the nanodiamond are mainly unknown. In this work, we examine the internal structure (crystalline and electronic) of one of the most popular DND hydrosols with positively charged colloidal particles through advanced TEM techniques. High-resolution TEM imaging and diffraction studies testified the crystalline diamond structure of the nanoparticles with the surface covered by a thin disordered layer (Fig. 10.2.11). Core-shell structure has been revealed for individual DND nanoparticles with a mean diameter of 4 nm by STEM-EELS imaging. The crystalline diamond core had a size of 2 nm and was surrounded by a "shell" of diamond-like carbon (DLC) with a thickness of »1 nm (Fig. 10.2.12).

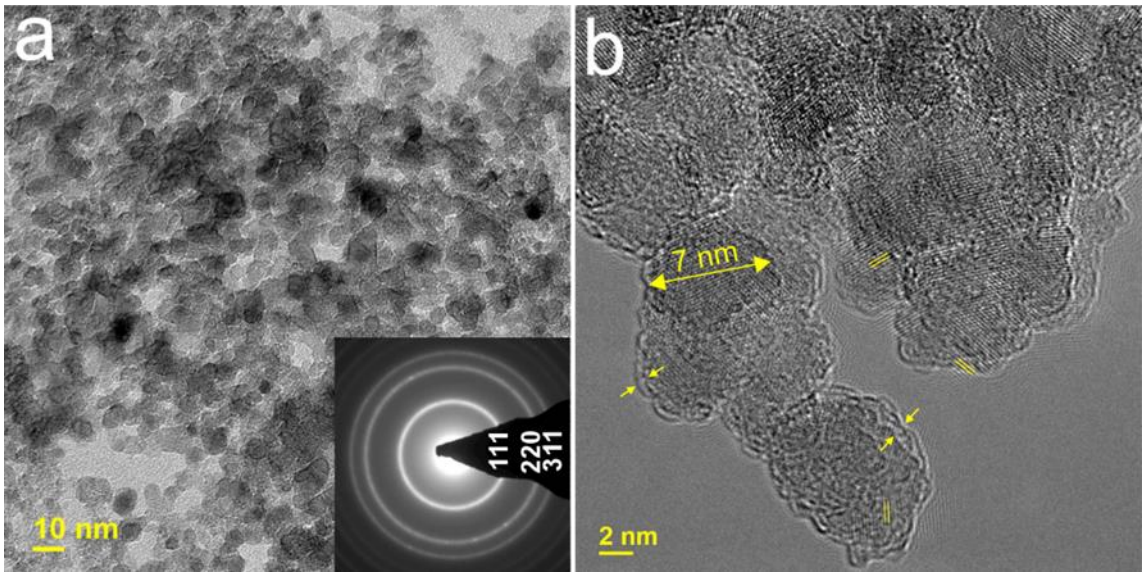

Figure 10.2.11 TEM images (a, b) and selected area electron diffraction pattern (inset) of DND particles annealed at 300°C. Some (111) planes of the diamond are marked with bars, while arrows indicate the disordered layer at the edge of the particles.

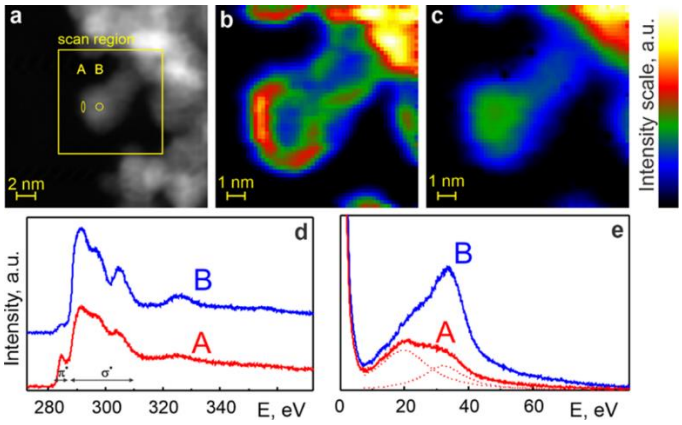

Figure 10.2.12. EELS analysis of individual DND particle at 300°C; (a) HAADF STEM image of the ROI. (b) and (c) EELS SI non-sp3 (b) and sp3 (c) carbon maps. Electron energy-loss spectra in the carbon K-edge region after background removal (d) and low-loss region (e) integrated over areas A in B shown in (a). Dot lines in Fig. 2e are two Lorentzian functions fitted to spectrum A.

Publication:

A.P.Kryshtal, N.O.Mchedlov-Petrossyan, A.N.Laguta, N.N.Kriklya, A.Kruk, E.Osawa, Primary detonation nanodiamond particles: their core-shell structure and the behavior in organo-hydrosols, Colloids and Surfaces A: Physicochemical and Engineering Aspects 2020, https://doi.org/10.1016/j.colsurfa.2020.126079

Mixing of Immiscible Components by the Size Effect: A Case Study of Au–Ni Nanostructures (KRA)

The nanoparticles consisting of several chemical elements, e.g. bimetallic ones, provide greater flexibility in tuning their properties and performance. Thus, Au-Ni core-shell or Janus-like morphologies combine catalytic or magnetic properties of Ni with plasmonic properties of Au, which is essential for applications in medicine and biotechnology, energy storage and conversion, chemical analysis, and catalysis. This work investigated the formation of solid solutions in Au–Ni nanoparticles using *in situ* TEM techniques. The curve limiting the components' solid-state miscibility gap was experimentally constructed in the whole concentration range at all temperatures. Significant shrinking of the solid-phase miscibility gap was observed for 6-nm-sized Au-Ni nanoparticles. Gold segregation to the surface of homogeneous nickel-based solid solution particles was witnessed. Furthermore, it has been shown that Au and Ni, which are immiscible in bulk, form a homogeneous solid solution at room temperature upon the reduction of size down to ≈2 nm. The resulting solid solution has a random alloy structure and provides long-term stability characteristics to equilibrium alloys.

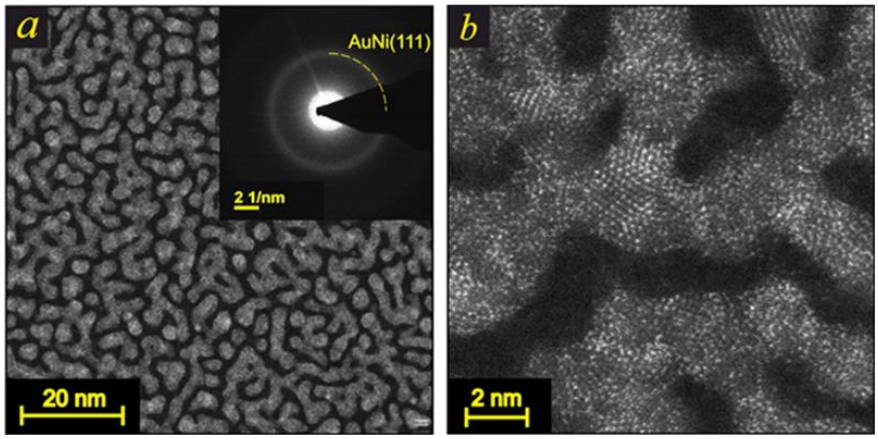

Figure 10.2.13. HAADF-STEM image of the Au-Ni film with a thickness of 1.3 nm (overview (a) and HR view (b)) formed on a C substrate at RT. The inset in (a) shows SAED pattern.

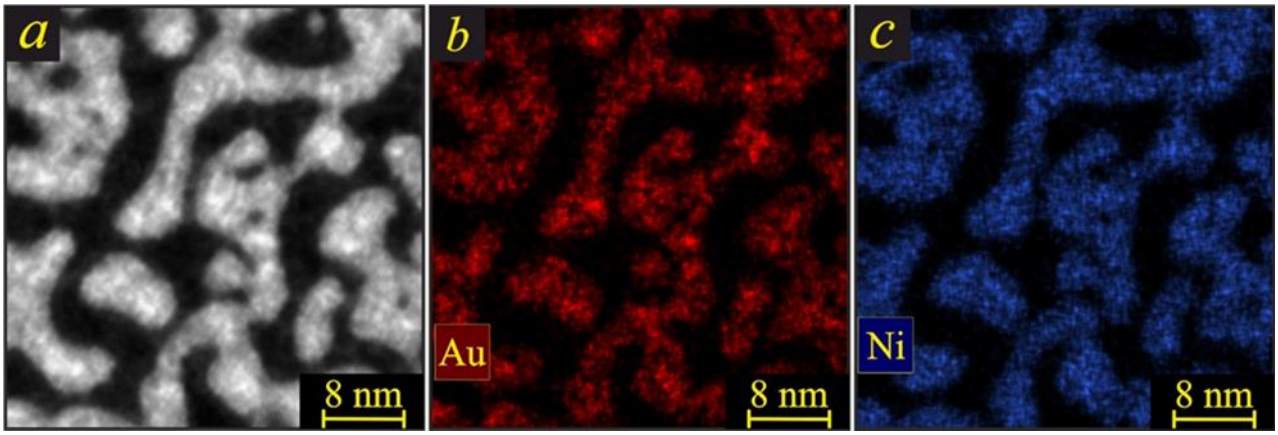

Figure 10.2.14. HAADF STEM image of the Au-Ni nanostructures with a size of 2 nm at room temperature and the corresponding EDX component distribution maps.

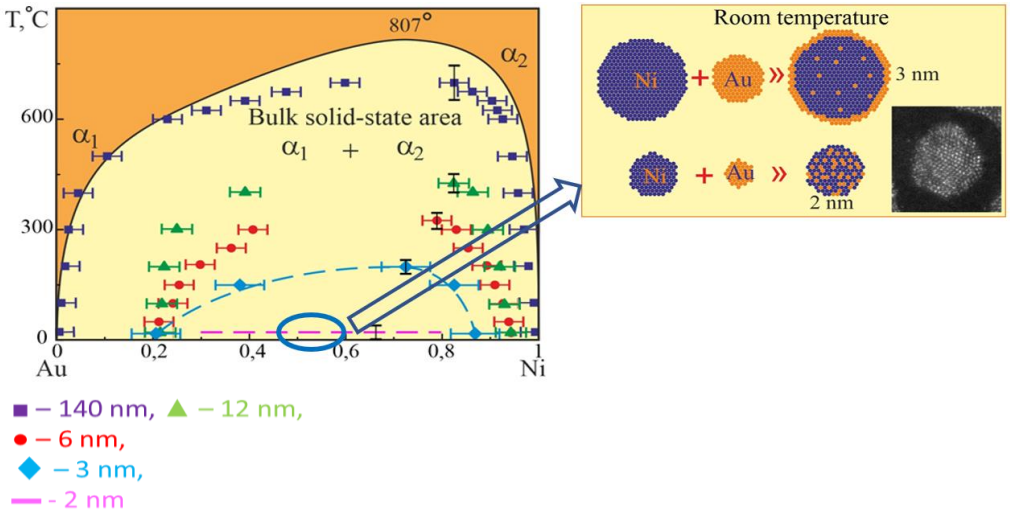

Figure 10.2.15. Size evolution of the solid-state miscibility gap in Au-Ni phase diagram.

Publication:

S. Bogatyrenko, A. Kryshtal, A. Kruk, O. Skryl, Mixing of Immiscible Components by the Size Effect: A Case Study of Au–Ni Nanostructures, J. Phys. Chem. C, 124, (2020) 25805−25811

https://doi.org/10.1021/acs.jpcc.0c06800

Effect of electron beam irradiation on the temperature of single AuGe nanoparticles in a TEM (KRA)

AuGe nanoparticles are used in photonic devices such as quantum dot infrared photodetectors, thermoelectric materials as well as materials for ion battery electrodes. Ge-Au nanoclusters embedded in silica are promising for phase change applications. In this work, we determined the temperature increment of single AuGe nanoparticles under electron beam irradiation in a TEM and a STEM. The nanoparticles were thermally cycled in an electron microscope in the 293-653 K temperature range, and the jump-like change of the morphology of the AuGe nanoparticles at melting was used as a temperature label (Fig. 10.2.16).

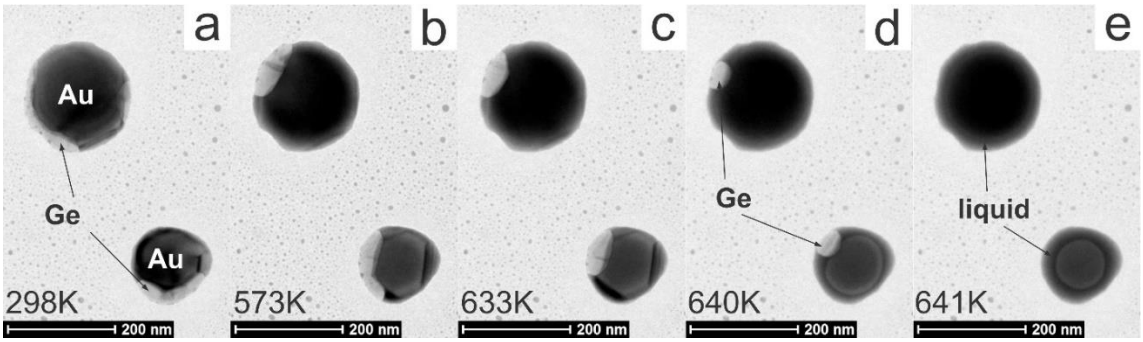

Figure 10.2.16. Bright-field TEM images of the same AuGe nanoparticles on the SiN_x membrane at different temperatures (a-e). Please note the jump-like disappearance of Ge upon the melting (e).

In the TEM, the temperature of a nanoparticle gradually rose with an increase of the beam current density, and the temperature increment reached 25 K at J ~ 1.8×10^6 A/m^2 (Fig. 10.2.17). The local temperature rise was calculated and analyzed within two independent approaches. It was shown that both models did not fit the experimental data under standard parameters (Fig. 10.2.17). No significant temperature increment of the AuGe nanoparticles was registered at conventional raster scans in a STEM mode with a beam current of up to 1 nA.

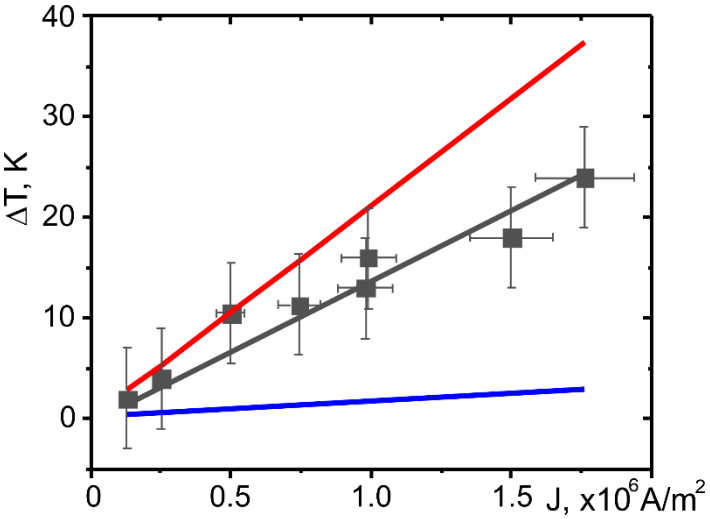

Figure 10.2.17. The temperature increment (ΔT) of the AuGe nanoparticles plotted as a function of the incident electron beam current density (J). The square points are experimental results of the current work (with a best-fit straight line). The red and blue lines are calculations according to the models [1] and [2], respectively.

1 L. Liu and S. H. Risbud, Realtime hot stage high voltage transmission electron microscopy precipitation of CdS nanocrystals in glasses: Experiment and theoretical analysis, J. Appl. Phys. 76 (1994) 4576-4580, https://doi.org/10.1063/1.357291

2 R. F. Egerton, P. Li, M. Malac, Radiation damage in the TEM and SEM, Micron 35 (2004) 399–409, https://doi.org/10.1016/j.micron.2004.02.003

Task 10.3: Materials for Automotive Body and Chassis structure (TRO, KRA)

Grain boundaries in 7xxx Al alloys (KRA, TRO)

The presented results are part of studies of grain boundaries in 7xxx Al alloys. We study precipitates at grain boundaries in an extruded AA7003 alloy, which is susceptible to stress corrosion cracking (SCC) [1]. Phase, size, shape and density of grain boundary precipitates and/or grain boundary density determine the SCC. The objective is to get more statistics of the different types of grain boundaries, preferably in 3D, the number and phase of precipitates, misorientation and the crystallographic nature of the grain boundaries. A high density of small precipitates at low angle grain boundaries (LAGB) was observed by FIB-SEM (Figure 10.3.1). By using higher magnifications in STEM, we can go more into details of the grain boundaries (Figure 10.3.2) showing three different types of grain boundaries. We also study the chemical composition of the particles at the grain boundaries, see figure 10.3.3.

[1] A Lervik, JC Walmsley, L Lodgaard, CD Marioara, R Johnsen, O Lunde, R Holmestad Stress corrosion cracking in an extruded Cu-free Al-Zn-Mg Alloy, Metals 2020, 10, 1194, https://doi.org/10.3390/met10091194

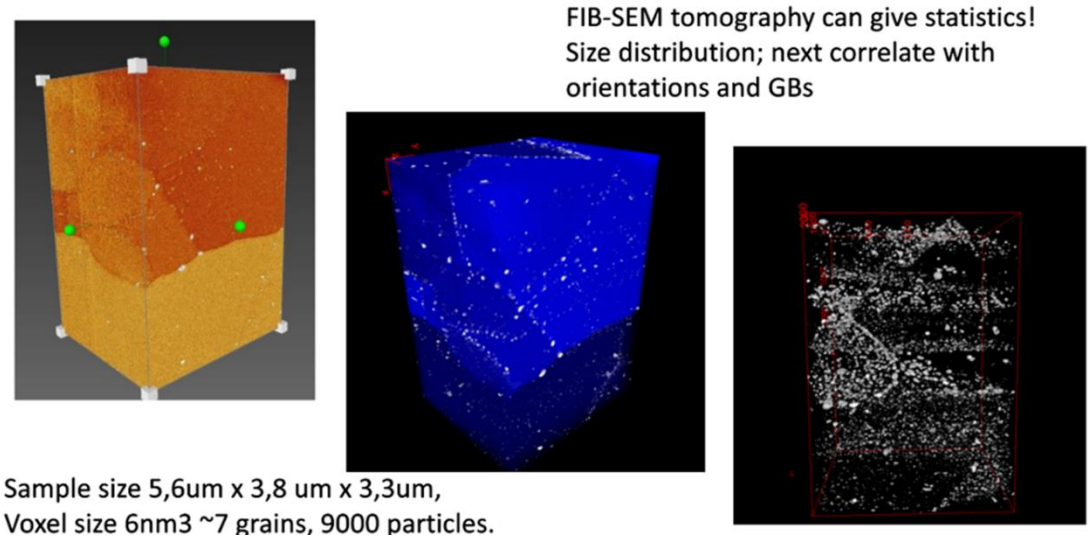

Figure 10.3.1. Visualization in 3D the particles precipitated at grain boundary in 7003 Al alloy.

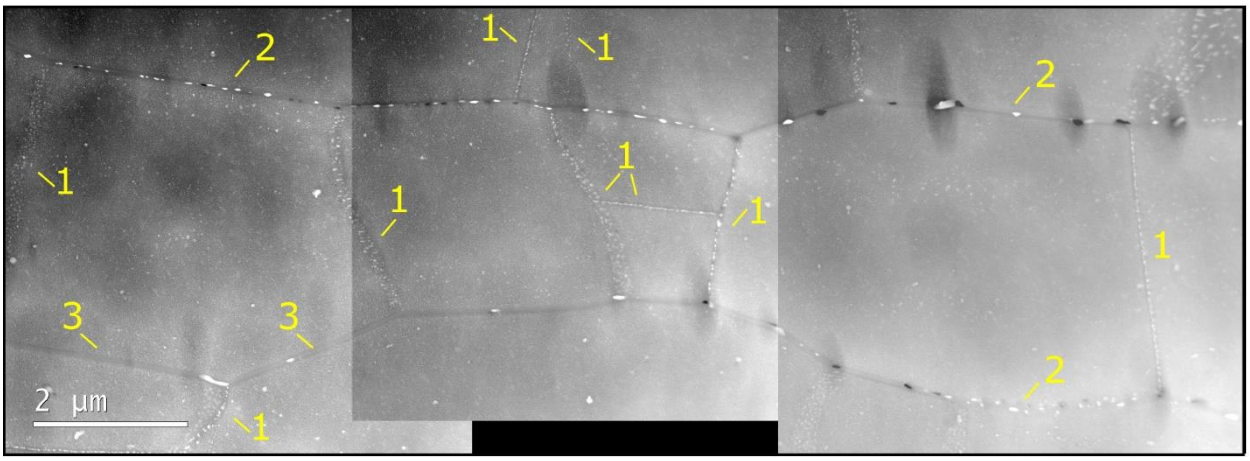

Figure 10.3.2. [1] HAADF-STEM image showing the typical microstructure found in TEM. Three distinct types of grain boundaries are observed. (1) Low-angle (< 2°) sub-grain boundaries with high number densities of particles. (2) Grain boundaries with fewer, but larger particles, and (3) grain boundaries with no or very few particles. The image is acquired parallel to the extrusion direction.

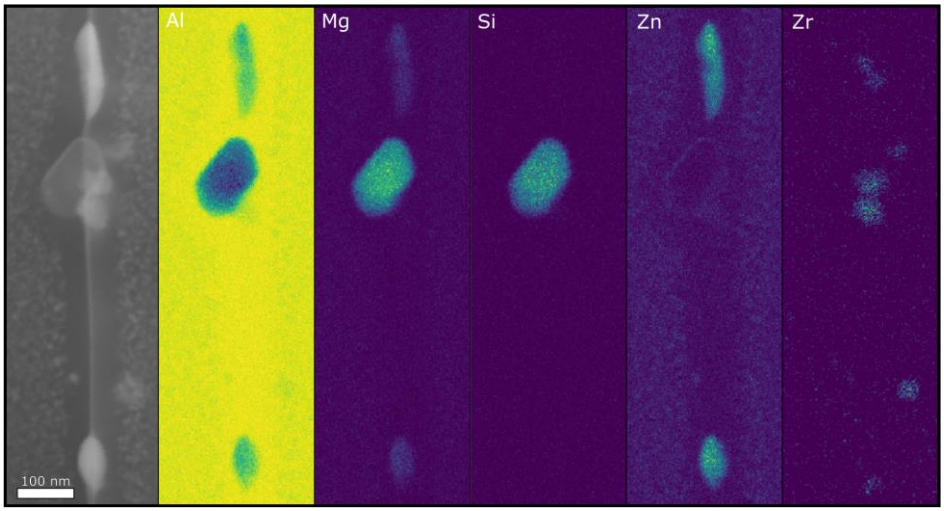

Figure 10.3.3.[1] A HAADF-STEM image and corresponding EDS maps from a grain boundary. Both MgZn2 and *η*-Mg2Si particles are present, if the material has been air-cooled. Al3Zr dispersoids are also found in connection with this grain boundary.

Development of experimental set up and data analysis routines for two-dimensional strain mapping by scanning precession electron diffraction technique (TRO, CAM)

Strain is an important parameter for tailoring the mechanical, electronic and optoelectronic properties of the functional and engineering materials. Investigation of local strain at higher spatial resolution requires techniques in the transmission electron microscope (TEM). Out of the available techniques for strain measurement in TEM, scanning precession electron diffraction (SPED) is the most convenient one. It is relatively easier to set up at the microscope, it does not require any additional configuration of the hardware and the scans can sample a large specimen area with reasonably good spatial resolution. However, though the data acquisition seems easy, data treatment and data analysis can be critical in obtaining a reliable output of strain analysis. In this work, a best practice routine for strain mapping with S(P)ED including experimental design and data analysis have been developed and justified. Influence of factors like (i) the beam/probe configuration (use of probe precession, beam convergence angle), (ii) the detection parameters (pixel size and pixel depth) and (iii) the analysis algorithms (cross-correlation, centre of mass method and Gaussian peak-fitting) on the strain map has been studied systematically. GaAs nanowire with a GaAsSb insert was used as a model system to establish the routine of strain analysis. A direct electron detector from Merlin medipix was used for fast and more sensitive data acquisition. Data acquired was treated and analysed with python-based package called pyXem. The routine developed was applied to characterize strain in the matrix of precipitation hardened Al 6xxx alloy.

The following presents some of the results of strain analysis as a function of a varying parameter in each case. The system used for this controlled study was GaAs nanowire with a GaAsSb insert, described in Fig 10.3.4. The nanowire has a Zinc Blend (ZB) GaAs structure below the insert and a Wurtzite (WZ) GaAs structure above the insert. In Fig 10.3.4, the nanowire is viewed in the $[1\bar{1}0]_{ZB}/[2\bar{1}\bar{1}0]_{WZ}$ orientation. The SPED scans for strain maps were acquired in the $[2\bar{1}\bar{1}]_{ZB}/[10\bar{1}0]_{WZ}$ orientation because of convenience of strain analysis.

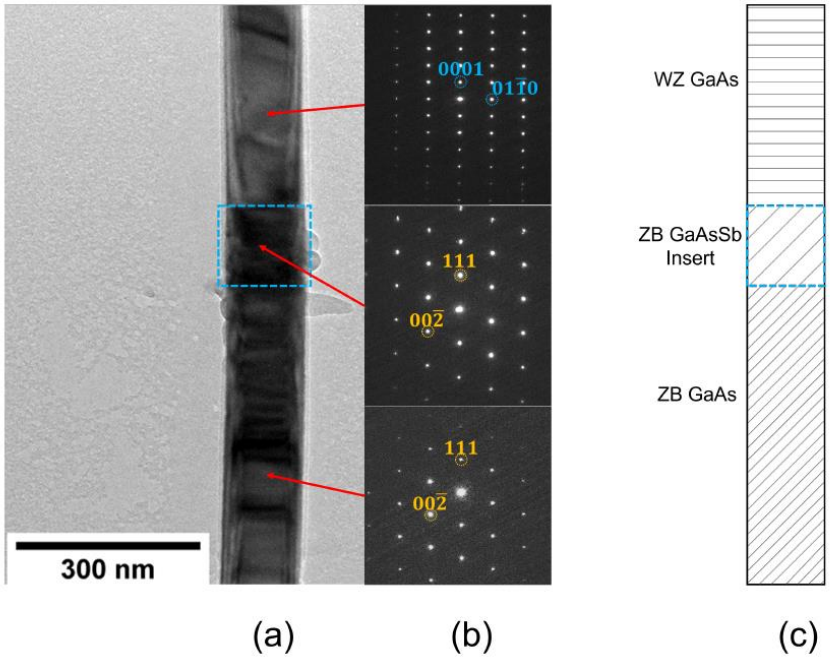

Figure 10.3.4. (a) shows the bright field (BF) image of the nanowire (NW) viewed in the $[1\bar{1}0]_{ZB}/[2\bar{1}\bar{1}0]_{WZ}$ orientation. The region marked by blue dotted box is the insert. (b) shows the diffraction pattern taken from the ZB, insert and WZ regions. (c) shows a schematic of the NW geometry.

Table 10.3.1 presents the different parameters of the sample, detector and the probe that have been used to take SPED scans and later see the effect on the strain analysis. Strain analysis from some of these scans are presented as follows.

Table 10.3.1. Conditions of the sample, detector and the probe used to take the different scans.

Scan	Region on zone	Pixel depth	Precession	Camera length[2]	Convergence angle[2]
Scan 1	Insert	12 bit	On	22.9 cm	0.077°
Scan 2	ZB just below insert	12 bit	On	22.9 cm	0.077°
Scan 3	ZB just below insert	6 bit	On	22.9 cm	0.077°
Scan 4	ZB just below insert	12 bit	Off	22.9 cm	0.077°
Scan 5	ZB just below insert	12 bit	On	37.2 cm	0.077°
Scan 6	ZB just below insert	12 bit	On	22.9 cm	0.244°

The strain analysis was done based on shift of a pair of selected diffraction spots in the x-direction and y-direction from the region around the insert with respect to that from a reference area away from the insert area. Fig 10.3.5 explains the methodology of strain analysis used in the work. The challenges involved in this methodology were as follows:

1. The wire was bent along its length. Hence, it was difficult to find the area around the insert and the reference area exactly on zone simultaneously.
2. During the different scans taken on the same region in the wire, contamination built up had happened which added noise in the diffraction data. This has proved to pose difficulty during the data analysis.

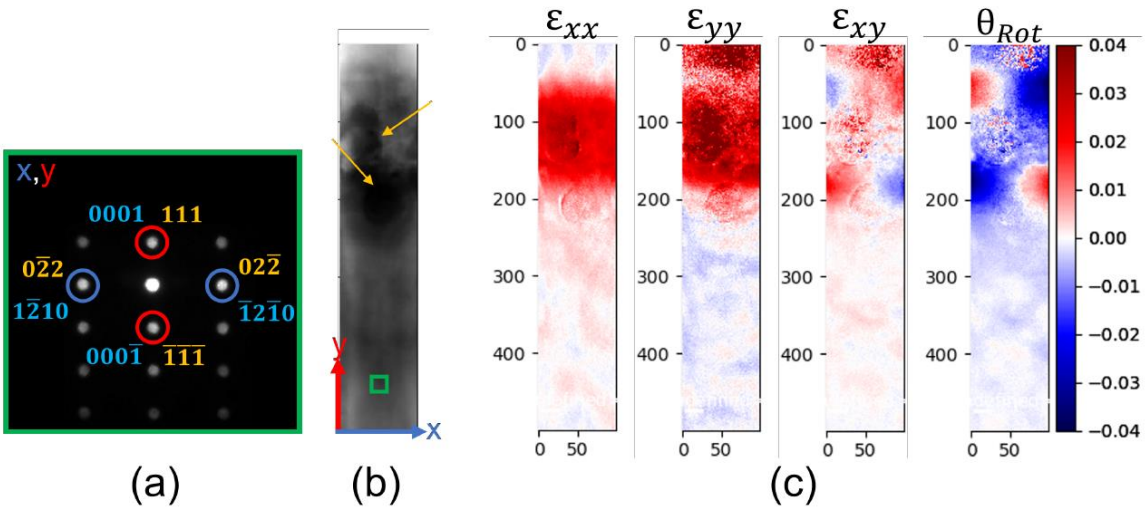

Figure 10.3.5. (a) shows the averaged diffraction pattern (DP) from 20x20 pixels in the presumably unstrained reference area, indicated by the green box in (b). x-direction spots are marked in blue circles and y-direction spots are marked in red circles. Indexing in yellow font is with respect to (wrt) ZB structure and that in blue font is wrt WZ structure. (b) shows the virtual bright field (VBF) image of the region scanned for strain mapping around the insert in scan 2, with the presumably unstrained region contributing to the averaged DP marked with a green square. Carbon contamination due to beam damage is marked by the yellow arrows. (c) shows the strain maps from the same region using cross-correlation method of peak-finding in the x direction, y direction, shear and rotation.

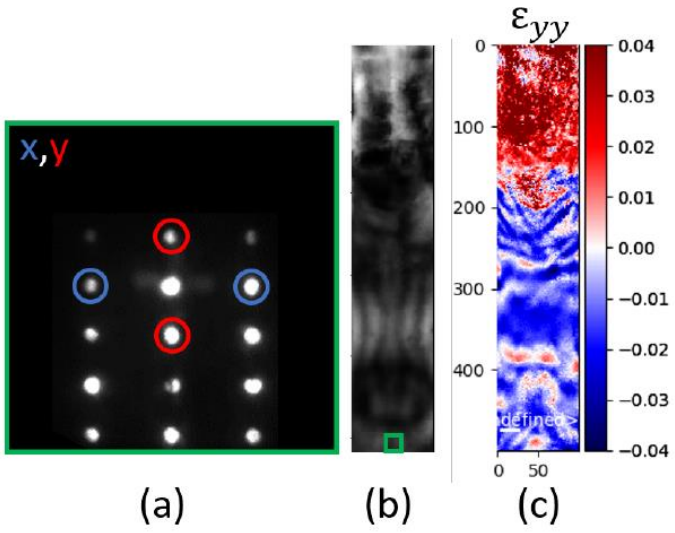

Figure 10.3.6. Strain mapping results from scan 4 (table 10.3.1) taken at precession angle ϕ = 0°. (a) shows the average DP from an unstrained area marked by the green box in the VBF image in (b). (c) shows the map of the normal strain in y-direction found by cross-correlation method.

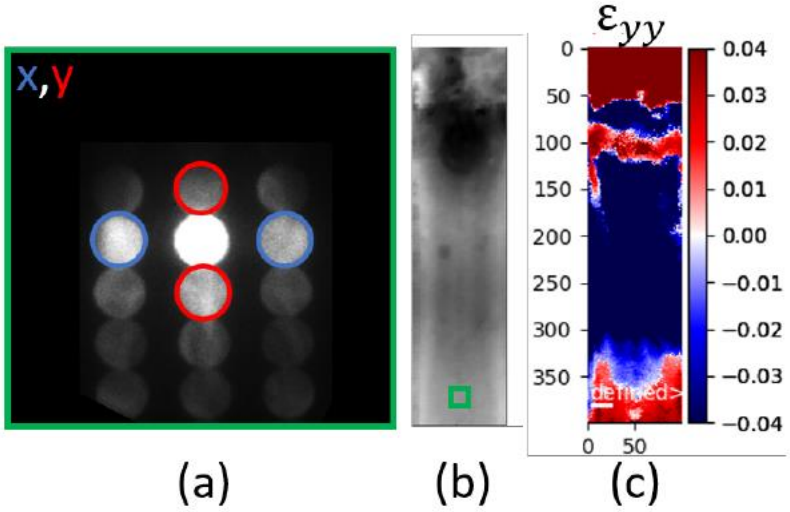

Figure 10.3.7. Strain mapping results from scan 6, which is taken with a larger convergence angle, α = 0.244°. (a), (b) and (c) have the same descriptions as in Fig 10.3.6, except for the current condition.

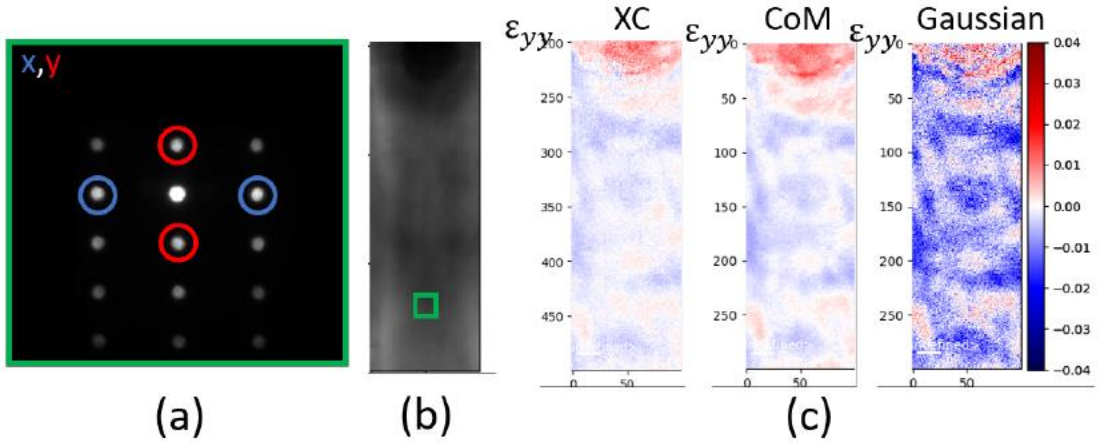

Figure 10.3.8. Comparison of the strain mapping routines performed on scan 2 (table 10.3.1) (a) shows the averaged DP from the reference area marked with a green box in the VBF shown in (b). (c) shows the resulting strain maps (normal y-direction strain) for the three routines on pyXem: cross-correlation, centre of mass and Gaussian fitting.

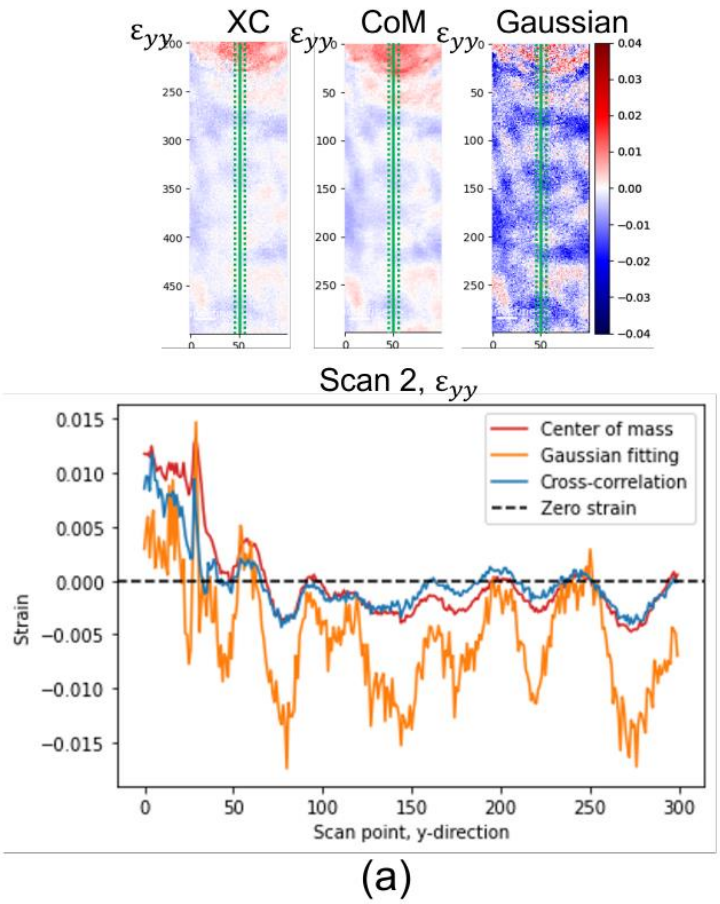

Figure 10.3.9. (a) shows strain maps and plotted line profiles for all the three strain mapping routines for the baseline case, scan 2.

Different control experiments were performed to lay out a best practice routine for two-dimensional strain mapping using SPED. The summary points of the study are:

1. Precession of the beam during the scan is beneficial in generating flat diffraction patterns such that the data analysis routines can be applied.

2. A convergence angle such that the diffraction discs do not overlap, and precession of the beam generated datasets, which could be analyzed sensibly with all the three peak finding routines on pyXem.

3. Straight samples are preferable for meaningful data analysis. Bent samples can be tricky, because the strain analysis can generate different results depending on if the insert area or the reference area was on zone.

4. The comparison between the three strain mapping routines on pyXem showed that the cross-correlation and the centre of mass methods often produced similar results. However, the centre of mass seems to be sensitive to which region of the sample is on zone if the sample is bent. The cross-correlation method, although seeming more robust, often produces lower strain values. The Gaussian method produced sensible strain behaviour inside the insert when it could be applied to the data but showed much larger

variations (low precision) in the regions assumed to be unstrained. All the three methods showed similar strain profiles, with peaks and valleys in the plotted lines at the same positions along the nanowire. This suggests that all the three methods pick up on the changes in the diffraction data but with different precision. The Gaussian fitting method was also limited by the quality of the data.

5. The cross-correlation method seems to produce the most robust strain results, when the sample contamination contributes to low signal-to-noise ratio. But for less noisy data, improved by background subtraction, the three different routines produced similar results.

6. The orientation for strain analysis should also be chosen with care such that the changes in the diffraction peak position is clear and easier to analyse.

The routines of strain analysis were also applied to SPED data from precipitation hardened Al-6xxx alloy and the preliminary results are presented in Fig. 10.3.10.

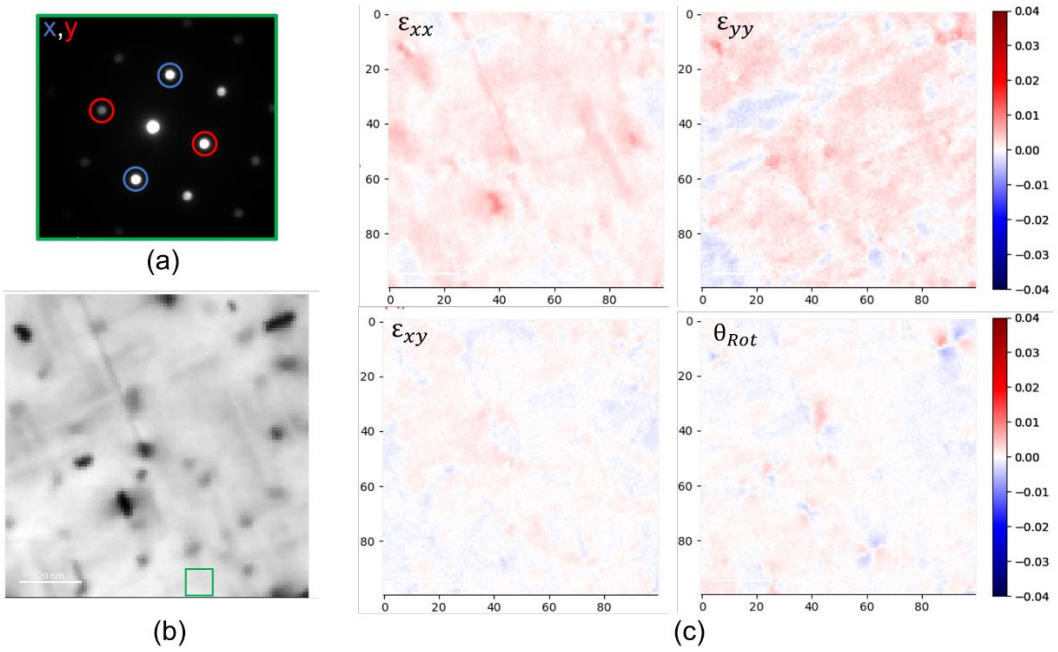

Figure 10.3.10. Preliminary strain mapping results done on SPED data from precipitation hardened Al-6xxx alloy. (a) shows the averaged SPED DP from the reference region with reflections for x- and y- directions marked by blue and red circles. (b) shows VBF image with reference area marked by a green square, (c) s a set of strain maps using the centre of mass method.

Publications:

1. NTNU Open: Strain mapping based on scanning (precession) electron diffraction of heterostructured semiconductor nanowires: set-up and analysis; Master's thesis by Ingeborg Nævra Prestholdt
2. Manuscript under preparation

Insights into secondary nucleation of precipitates on alpha-dispersoids of Al-Mg-Si-Cu alloy (TRO, KRA)

Precipitation in Al matrix increases the strength of the alloy. The Cu containing alloy contains Cu in the precipitate. Sometimes, precipitates also nucleate on the dispersoids instead of the matrix in Al and this phenomenon is called secondary nucleation of precipitates. It is a common phenomenon and occurs during heat treatment of the Al alloys. Secondary nucleation reduces the strength of the alloy, because it 'steals' the hardening materials (precipitates and solutes) from the matrix on to the dispersoids. In this study, it has been attempted to understand secondary nucleation as a function of different heat treatments. Advanced high-resolution scanning transmission electron microscopy (STEM) and FIB-SEM tomography techniques have been employed to understand the secondary nucleation phenomenon. It is interesting to observe how the heat treatments affect secondary nucleation and the insights gained through the study can be used in directing treatment of alloys such that secondary nucleation is minimized and strengthening of alloys can be facilitated.

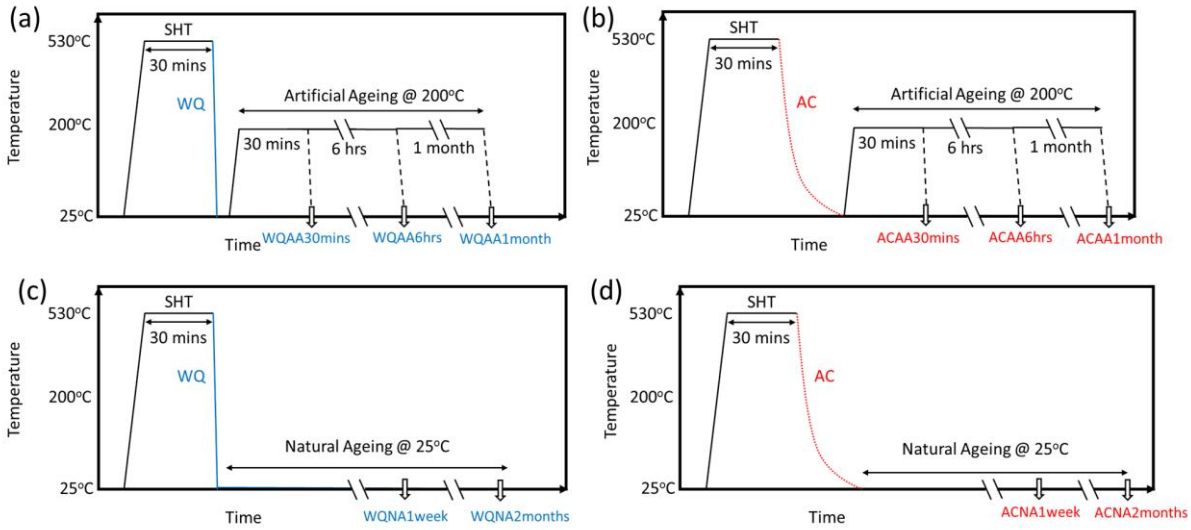

Figure 10.3.11. Schematic showing the different heat treatments done on the alloy. Four blocks of alloys were solution heat treated (SHT) at 530°C for 30 mins. One block was water quenched and then artificially aged at 200°C and samples were collected after 30 mins, 6 hrs and 1 month of artificial aging as illustrated in (a) with sample names. Another block was air cooled and artificially aged at 200°C. Three samples were collected after 30 mins, 6 hrs and 1 month, as illustrated with sample names in (b). A third block was water quenched and left for natural aging at room temperature and samples were collected after 1 week and 2 months of natural aging, as illustrated with sample names in (c). A fourth block was air cooled to room temperature and was left for natural aging at room temperature, as illustrated with sample names in (d).

The different heat treatments and the sample names are illustrated in Fig 10.3.11. The samples, heat treated differently were imaged to obtain statistics about secondary nucleation from about 30 dispersoids from each set.

Broadly, the air-cooled samples were observed to have large secondary precipitation on the dispersoids and the water quenched samples were observed to have much finer secondary precipitation on the dispersoids, as shown in Fig 10.3.12. A higher magnification image in Fig 10.3.13 (a) shows the precipitates growing on the dispersoid clearly. The structure of the precipitation was found to be often disordered, as seen in Fig 10.3.13 (b). The naturally aged samples were interesting, specially post water quenching. Energy dispersive spectroscopy (EDS) from the dispersoids from WQNA_1week showed segregation of Cu around the dispersoid, showing an early stage of diffusion of Cu atoms at the junction of the dispersoid and the Al matrix (Fig 10.3.14).

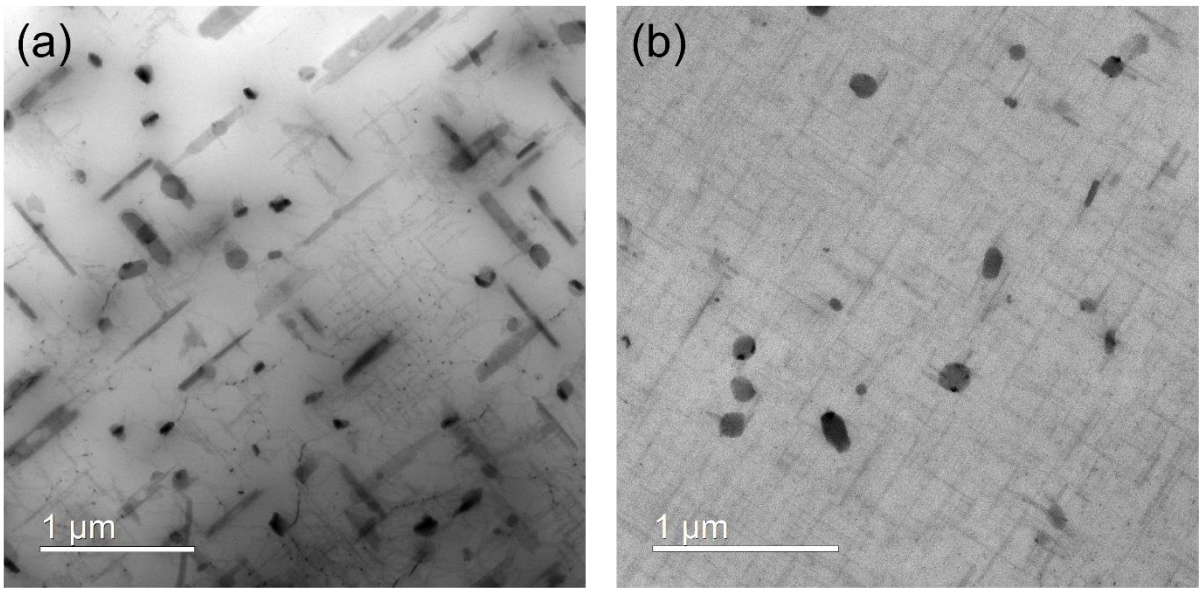

Figure 10.3.12. (a) shows the bright field (BF) STEM image of the alloy ACAA_1month and (b) shows the BF STEM image of the alloy WQAA_1month.

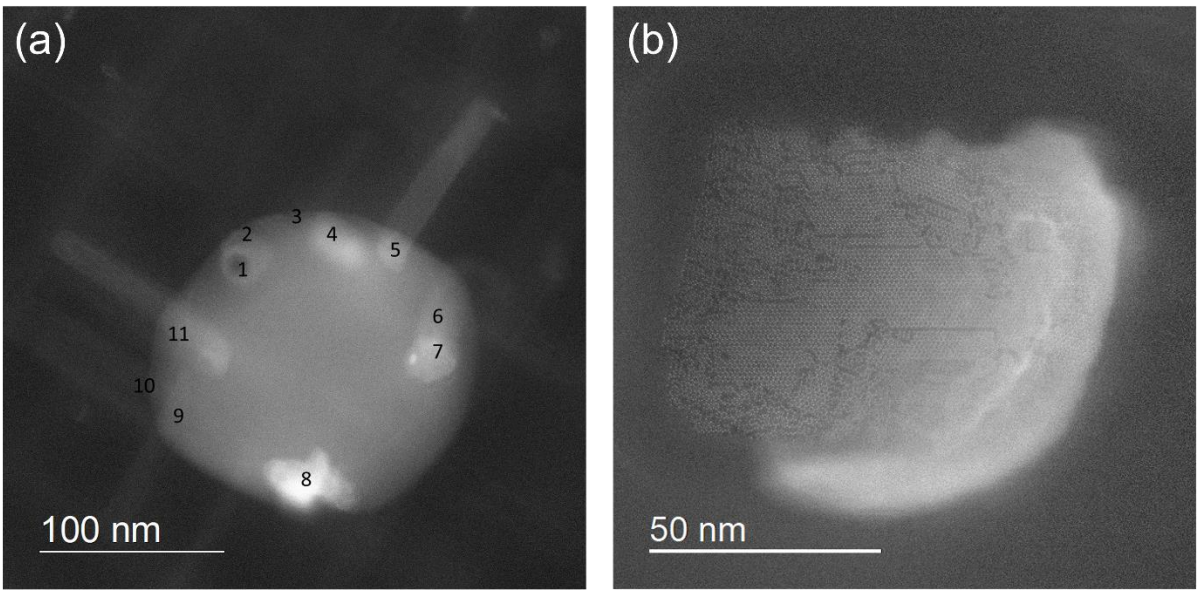

Figure 10.3.13. (a) BF TEM image of a dispersoid on which secondary nucleation of precipitates have happened. The precipitates are numbered in the figure. (b) High resolution STEM of the secondary precipitate on a dispersoid showing that the precipitate has pockets of disordered structures.

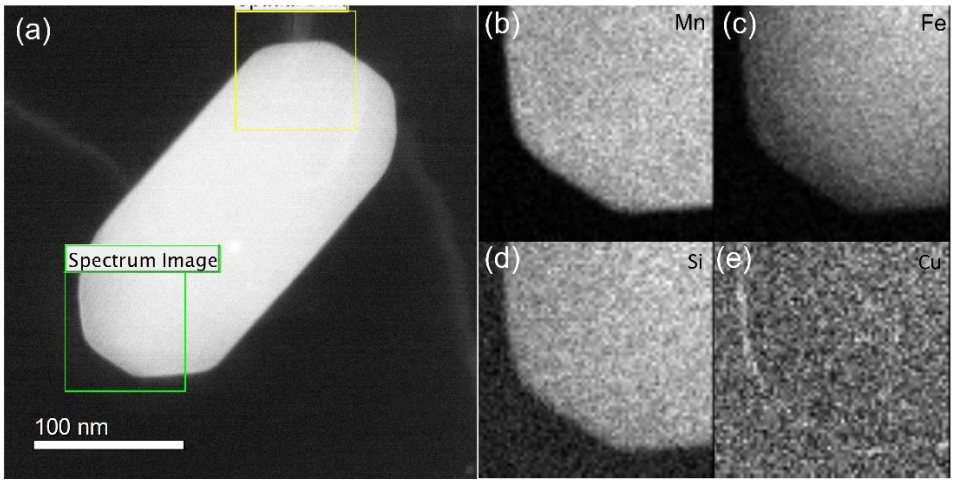

Figure 10.3.14. EDS map from a dispersoid of WQNA_1week sample. The region of interest (ROI) is marked in (a), maps of Mn, Fe, Si and Cu are presented in (b), (c), (d) and (e) respectively. The map for Cu shows segregation of Cu around the dispersoid.

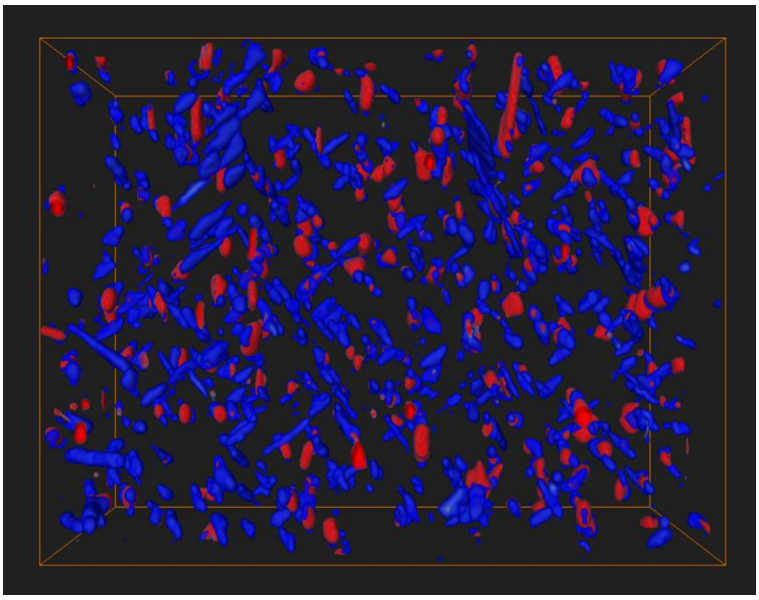

Figure 10.3.15. FIB-SEM tomography of ACAA_1month sample separating the dispersoids and the precipitates

FIB-SEM tomography from some of the key samples are conducted in collaboration with the team in Krakow to obtain better statistics from a larger volume of the sample (Fig. 10.3.15).

The work will be continued with focus on the following directions:

1. Quantitative analysis of the FIB-SEM data from air-cooled and water quenched treatments to get better statistics on the volume of secondary nucleation on the dispersoid in the two cases.
2. Overlaying atoms on the disordered precipitates to conclude about the structure of the precipitates.
3. Qualitative analysis of the HR STEM data acquired from the different heat treatment conditions to get insight on the evolution of secondary nucleation as a function of ageing time.

Effect of the nanostructuring by high-pressure torsion process on the secondary phase precipitation in UNS S32750 Superduplex stainless steel (TRO)

In this work, the precipitation and the morphology of secondary phases after severe plastic deformation (SPD) processing followed by an isothermal treatment was investigated. High-pressure torsion (HPT) was the SPD process carried out on superduplex 2507 (UNS S32750) stainless steel material under P = 6 GPa at room temperature. At this high strain levels (ε up to 170) samples have shown grain size decrease and strained microstructure with high dislocation density and nanostructure features. After a short isothermal treatment at 830^{o}C, the sigma phase and chromium nitrides were revealed as the main secondary phases identified by scanning and transmission electron microscopy and element analysis by energy dispersive spectroscopy. Scanning precession electron diffraction and automated crystal orientation mapping have been

carried out in order to confirm the precipitation of the secondary phases. In fact, the results provide evidence that the precipitation of chromium nitrides seems to be the preferred nucleation site for sigma phase at higher deformation strain, in addition to the intergranular precipitation of sigma. Both the sigma phases nucleated inter-granularly and besides chromium nitrides are randomly orientated.

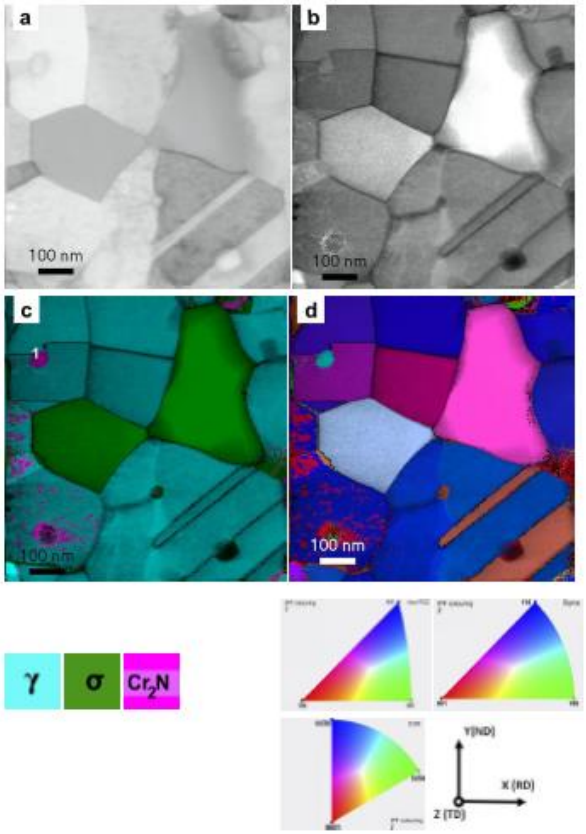

Figure 10.3.16. SPED scan area for a sample at one of the experimental conditions: (a) VBF, (b) Indexed image (c) phase map of austenite (cyan), Chromium nitride (purple) and sigma (green), (d) orientation map of the three phases in Z direction. Phase color identification and directions considered for the samples and the inverse pole figure coloring for each phase are shown at the bottom.

Publication:

Effect of the nanostructuring by high-pressure torsion process on the secondary phase precipitation in UNS S32750 Superduplex stainless steel; Alisiya Biserova-Tahchieva*, Dipanwita Chatterjee, Antonius T. J. van Helvoort, Núria Llorca-Isern, Jose Maria Cabrera, Just accepted manuscript in Materials Characterization, Elsevier

Identification of clusters and precipitate phases and understanding their nucleation in Al alloys by SPED and STEM (TRO, CAM)

Age-hardenable aluminium – Al-Cu, Al-Mg-Si and Al-Mg-Zn– alloys are important structural materials for automotive applications due to properties like high strength/weight ratio and good formability, often combined with good corrosion resistance. Chemical composition and thermo-mechanical history of the alloy will to a large extent decide its physical properties. The TEM group in Trondheim has over a long period worked together with the Norwegian light metal industry on nanoscale studies of aluminium alloys [1]. The combination of high angle annular dark field scanning transmission electron microscopy (HAADF-TEM) and scanning (precession) electron diffraction (S(P)ED) constitutes a strong toolbox to learn more about aluminium alloys and the correlation between micro/nano-structure and properties. HAADF-STEM maps the atomic structure of clusters and precipitates and predicts how they develop, while SPED can give information of phase fractions and orientation relationships from larger areas and provide the statistics needed. We can then design new or optimize chemical compositions of existing alloys to get desired properties for given applications [2].

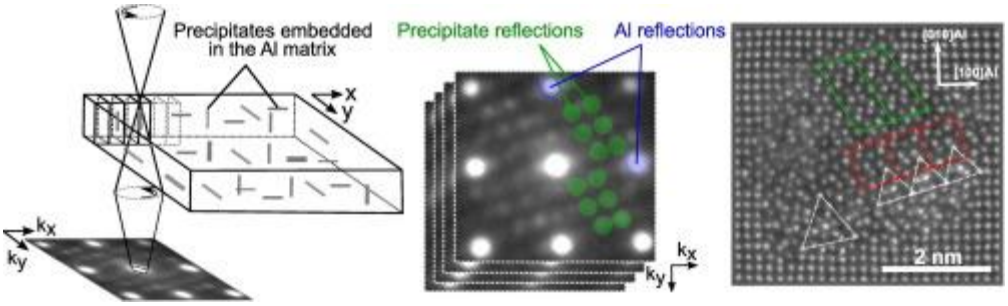

Figure 10.3.17. [3] Overview of the technique used to determine phase fractions and statistics of precipitates in age-hardenable aluminium alloys.

The HAADF-STEM experiments are done on a double corrected coldFEG JEOL ARM200 and the SPED experiments are performed on a JEOL 2100F equipped with a Quantum Detectors Merlin direct electron detector. Hyperspy [3] is used for analysis of the 4D SPED datasets.

We have recently proposed the structure of the main clusters, the so-called GPI zones, in Al-Zn-Mg alloys [4] and found that they are composed of one fundamental basic unit. This is essentially a partial substitution by Mg and Zn on an fcc unit cell and a surrounding truncated cube octahedral (TCO) shell with a possible interstitial at the centre of the TCO. The TCO units arrange in certain directions according to simple principles to form larger clusters, as shown in Figure 10.3.18 a) and b). The virtual dark-field image obtained from a SPED data stack shows a fine dispersion of clusters in the Al-Zn-Mg alloy. Due to the small size of the clusters, the cluster/Al signal ratio in the diffraction patterns is low [5]. To increase the signal, the diffraction patterns in all pixels belonging to a single cluster can be added, as shown in Figure 10.3.18 c). From the virtual dark-field image, we are investigating the possibility of extracting size and density of the clusters. Compared to the Al-Mg-Zn and Al-Cu systems, HAADF-STEM imaging is much more challenging for the Al-Mg-Si system, because of the similar Z contrast from all atoms. S(P)ED combined with simulation of diffraction patterns has become a powerful technique for elucidating the structure of the clusters (which are still unknown) and quantify precipitates in the age-hardenable aluminium alloys. The improved understanding gained in this work helps in designing new alloy processing routines that may achieve better combinations of properties in Al alloys.

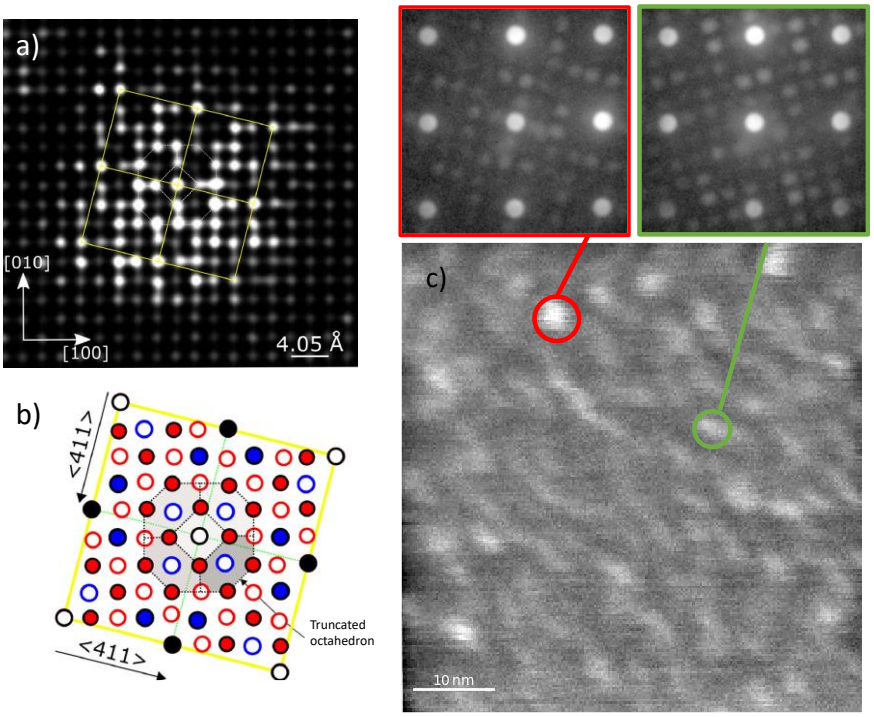

Figure 10.3.18. a) Filtered HAADF-STEM image of a cluster in an Al-Zn-Mg alloy. b) Corresponding suggested atomic column maps [4] c) Virtual dark-field image obtained from a SPED data set showing a fine dispersion of clusters, with corresponding diffraction patterns from two clusters.

References:

[1] Andersen SJ, Marioara CD, Friis J, Wenner S, Holmestad R, Precipitates in aluminium alloys, Adv. in Phys. X, 3:1, 1479984 (2018), https://doi.org/10.1080/23746149.2018.1479984; Saito T, Mørtsell EA, Wenner S, Marioara CD, Andersen SJ, Friis J, Matsuda K Holmestad R. Adv. Eng. Mater. 20, 1800125 (2018). https://doi.org/10.1002/adem.201800125.

[2] Sunde JK, Marioara CD, van Helvoort, ATJ, Holmestad R. The evolution of precipitate crystal structures in an Al-Mg-Si(-Cu) alloy studied by a combined HAADF-STEM and SPED approach, Mat. Char., 142, 458 (2018), https://doi.org/10.1016/j.matchar.2018.05.031

[3] de la Peña F, Prestat E, Fauske VT, Burdet P, Lähnemann J, Furnival T, Jokubauskas P, Nord M, Ostasevicius T, MacArthur K, Johnstone DN, Sarahan M, Aarholt T, Taillon J, Migunov V, Eljarrat A, Caron J, Poon T, (2021). hyperspy/hyperspy: Release v1.6.5 (v1.6.5). Zenodo. https://doi.org/10.5281/zenodo.5608741

[4] Lervik A, Thronsen,E, Friis J. Marioara CD, Wenner S, Bendo A, Matsud, K, Holmestad R, Andersen SJ. Atomic structure of solute clusters in Al-Zn-Mg alloys. Acta Mat. 205, 116574 (2021). http://dx.doi.org/10.1016/j.actamat.2020.116574.

[5] Thronsen E, Frafjord J, Friis J, Marioara CD, Wenner S, Andersen S, Holmestad, Submitted (2021)

[6] Thronsen, Bergh, Christiansen, Crout, van Helvoort, Midgley, Holmestad (2021) work in progress